



Bi-stable cross-flow pendulum at high Reynolds numbers: experimental investigation and stochastic modelling

Di Bao¹ , Nicolas Plihon¹  and Mickaël Bourgoïn¹ 

¹CNRS, ENS de Lyon, LPENSL, UMR5672, Lyon F-69342, France

Corresponding author: Di Bao, di.bao@ens-lyon.fr

(Received 13 September 2024; revised 30 January 2025; accepted 30 January 2025)

The bi-stable dynamics of a one-degree-of-freedom disk pendulum swept by a flow and allowed to rotate in the cross-flow direction is investigated experimentally. For increasing flow velocity, a subcritical bifurcation is observed from a Pendulum state, characterised by an increasing time-averaged pendulum angle with large amplitude fluctuations, to a rotating state with a non-zero mean rotation velocity at a critical free stream velocity U_{P2W} . The rotating state, referred to as Windmill state, presents a strong hysteresis: once initiated, it is sustained down to velocities $U_{W2P} < U_{P2W}$ before bifurcating towards the Pendulum state. A thorough experimental characterisation of the dynamical features of each state is reported, with a particular focus on the influence of the static yaw angle of the disk β_0 and the free stream velocity. In the Pendulum state, the system behaves differently depending on whether β_0 lies below or above the stall angle of the disk, with more regular dynamics below. We demonstrate that the bifurcation between the Pendulum state and the Windmill state is triggered by aerodynamic fluctuations, while the bifurcation between the Windmill state and the Pendulum state is deterministic. A stochastic model faithfully reproduces the dynamical features of both states, as well as the characteristics of the bifurcations.

Key words: flow–structure interactions

1. Introduction

The pendulum is one of the most fundamental dynamical systems studied in physics and engineering. Its simplicity and analogy with ubiquitous oscillatory systems in natural and industrial environments make it a valuable model for understanding various physical

phenomena. This is particularly the case in the field of fluid mechanics when a pendulum is coupled with its surrounding fluid.

In quiescent fluids, the pendulum serves as a tool for introducing the added mass concept (Stokes 1850; Neill, Livelybrooks & Donnelly 2007). Recently, the wake created by underwater heavy pendulums (cylindrical in Mathai *et al.* (2019) and spherical in Gold *et al.* (2024)) was found having a strong disturbing effect on the pendulum oscillation.

In fluid flows, additional complexity and intriguing dynamical behaviours are introduced to the pendulum. A large volume of previous studies focused on the flow-induced vibrations of underwater pendulums, extensively applied for underwater towing systems. When the flow is in the direction of gravity, the dynamics of pendulums immersed in two-dimensional (2-D) flowing soap films recently raised attention: an instability towards a spontaneous oscillatory regime for flexible pendulums (Bandi *et al.* 2013), as well as for rigid pendulums (Orchini, Kellay & Mazzino 2015), whose origin is attributed to the galloping instability. When the flow is vertical to the direction of gravity, the vortex-induced vibration (VIV) of a tethered 2-D cylinder with positive buoyancy was investigated by Ryan *et al.* (2004, 2007) numerically and by Carberry & Sheridan (2007) experimentally, highlighting a sudden transition from in-line to transverse oscillation with increasing free stream velocity. This transition exhibits a strong coupling with a change in the cylinder wake dynamics. The confinement ratio between the sizes of a 2-D tethered cylinder and a water channel is found from Fani & Gallaire (2015) to have a strong influence on the type of instability, with a transition from a confinement-induced instability (Semin *et al.* 2012) to a confinement-induced divergence as this ratio decreases. With an increase in geometrical complexity to three-dimensional (3-D) configurations, a tethered sphere exhibits far more complex VIV, driven by multiple wake modes (Govardhan & Williamson 1997; Rajamuni, Thompson & Hourigan 2019; Kovalev *et al.* 2020, 2022; Kovalev, Eshbal & Van Hout 2022). Finally, the response of pendulums to oscillatory flows and waves are important in the contexts of offshore structures and energy harvesting systems (Bos & Wellens 2021).

In recent years, the interactions between pendulums and air flow have begun to receive more attention. A thin-disk pendulum facing a flow and freely rotating in the flow direction shows sudden transitions in pendulum angle with the incident flow velocity (Obligado, Puy & Bourgoïn 2013), caused by the sharp stall observed for 3-D geometries. These transitions were later analysed in the framework of rare-event statistics (Gayout, Bourgoïn & Plihon 2021). In the context of rotation in the cross-flow direction, a cube pendulum, mimicking a cabin for cable transport with a bad aerodynamic design, is potentially subject to the galloping instability (Myskiw *et al.* 2024).

Those previous studies enriched greatly our understanding on the fluid–structure interactions of pendulum systems, showing typical pendulum dynamics with complex one- or two-degree-of-freedom oscillations around a mean position. In the present work, we focus on a thin-disk pendulum with one degree-of-freedom in the cross-flow direction, presenting bi-stability with two stable states: the typical Pendulum state, reported in previous studies and observed for low flow velocities, and a Windmill state observed at high flow velocity presenting an unexpected autorotation behaviour (Lugt 1983). These features, to the best knowledge of the authors, have never been investigated or revealed before from an aerodynamic point-of-view. This study could raise potential interests for the field of turbomachinery or wind-energy harvesting when the mass of the rotatory devices is imbalanced due to manufacturing mistakes or structural damage (Ramlau & Niebsch 2009; Gong & Qiao 2012). In particular, we analyse in depth the influence of the yaw angle of the disk on the features of both the Pendulum and the Windmill states.

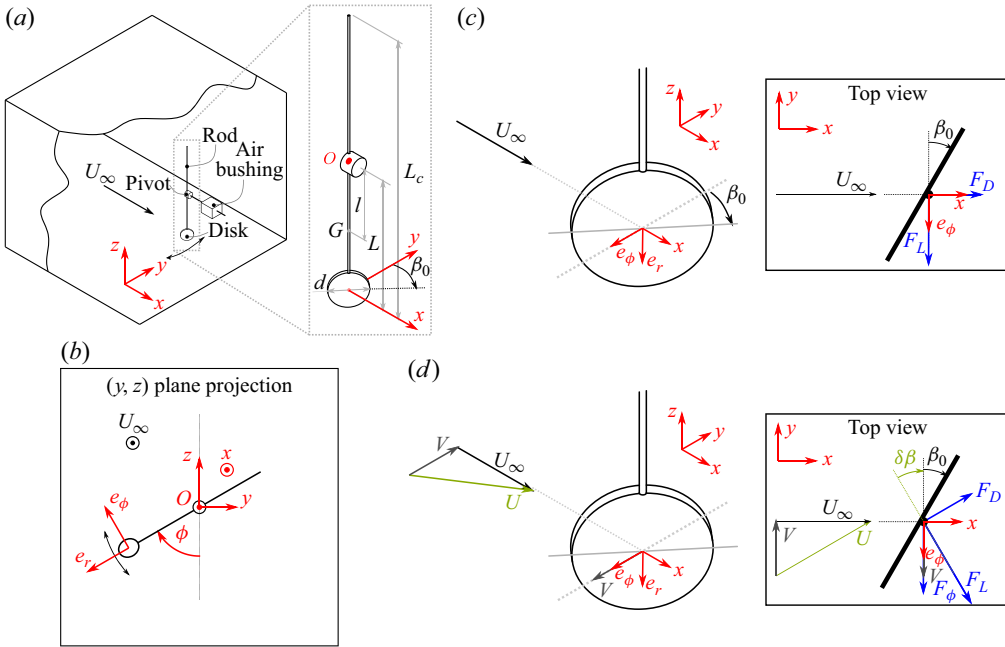


Figure 1. (a) Arrangement of the pendulum system in the test section. (b) Projection of the pendulum system in the (y, z) plane illustrating the definition of the cylindrical coordinate system, where e_ϕ and e_r represent the unit vector along the azimuth (ϕ) and axial (r) directions, respectively. (c,d) Zoomed view near the disk (c) without and (d) with motion. The specific case at $\phi = 0^\circ$ (for which e_ϕ is parallel to y) is chosen in (c) and (d) for better presentations of the static yaw angle (β_0) and the dynamical yaw angle ($\delta\beta$). The thickness of the disk is magnified by a factor of 10 for clarity.

The paper is structured as follows. The experimental methodology is detailed in § 2. Results in § 3 first present an overview of the dynamical states and their transitions in § 3.1, followed by a detailed investigation of the system dynamics in different states in § 3.2. These main results are further discussed in § 4, with the help of a simple stochastic model, and are finally summarised in § 5.

2. Experimental set-up

2.1. Wind tunnel facility, pendulum system and measurement techniques

The experiments are conducted in a close-loop wind tunnel at ENS de Lyon. The length of the test section having a $51 \times 51 \text{ cm}^2$ square cross-section is 4 m. At most operating conditions, the turbulence intensity of the incoming flow is of the order of 2%. In figure 1(a), an isometric view of the arrangement inside the test section is shown. A Cartesian coordinate system is defined with x in the streamwise direction, y in the horizontal direction and z in the vertical direction. An air-bushing system (OAVTB16i04 from OAV Labs) is positioned at the centre of a plane 2 m downstream of the inlet of the test section. It enables frictionless rotation of a shaft parallel to the flow direction. A cylindrical carbon-fiber rod of diameter $d_c = 2 \text{ mm}$ and length $L_c = 33 \text{ cm}$ is attached perpendicularly to the shaft, in the transverse plane. At one end of the rod, a thin aluminium disk is attached. It has a diameter of $d = 4 \text{ cm}$ and a thickness of 0.4 mm . The total mass of the pendulum is $m = 2.73 \text{ g}$ (1.21 g from the rod and 1.52 g from the disk). The ensemble constitutes a simple one-degree-of-freedom pendulum susceptible to rotation in a plane perpendicular to the mean free stream. As shown in

figure 1(b), a cylindrical coordinate system (r, x, ϕ) is defined, with the origin O located at the centre-of-rotation and ϕ being the angle between the pendulum and the vertical axis z .

The blockage ratio of the whole pendulum system is calculated to be 1.2 %, making further considerations on the blockage effect unnecessary. Furthermore, according to the experiments by Ruiz *et al.* (2009) on a disk fixed to a wall, the disk wake was found to be only slightly modified by the wall when the distance between the disk and the wall is at the maximum value considered in their study: $1.75d$ (d is the diameter of the disk). In addition, the experiments by Ramamurthy & Lee (1973) on 2-D cylinders (having equilateral triangle or circular cross-section) suggest that the wall effect can be neglected when the distance from the cylinder to the wall is larger than twice the characteristic length of the cylinder. Therefore, the distance L from the centre of the disk to the pivot is adjusted to 15 cm to have the distance between the disk and the wind-tunnel wall always larger than $2d$. Finally, calculated from the mass distribution around the centre-of-rotation, the distance from the centre-of-mass to the pivot is $l = 8.1$ cm and the moment of inertia is $J = 4.51 \times 10^{-5}$ kg m². As will be presented in detail later, in the Pendulum state, the pendulum oscillates around a non-zero equilibrium angle $\bar{\phi}$, which is due to the balance between aerodynamic torque and the gravitational torque. By linearising the equation of motion around a mean angle $\bar{\phi}$ (will also be presented later in § 4.1), it can be found that the natural frequency is $f_0 = \frac{1}{2\pi} \sqrt{\frac{mgl}{J} \cos(\bar{\phi})}$, where $\bar{\phi}$ is the mean pendulum angle and $g = 9.81$ m s⁻² is the gravitational acceleration. The frequency is at its maximum when $\bar{\phi} = 0$ (without wind) and is calculated to be 1.1 Hz.

Based on the above-described experimental set-up, two control parameters are considered in the present work.

The first parameter is the free stream velocity U_∞ , which is set by the rotation frequency of the motor driving the fan of the wind tunnel and externally controlled using an analogue output of a National Instrument multifunction I/O data acquisition (DAQ) module PXI-6229. The aerodynamic conditions are monitored by a combination of measurements of dynamic pressure, atmospheric pressure and temperature. They are measured at a location 30 cm upstream of the pendulum using a pitot tube and a thermocouple. In this work, we consider a U_∞ range from 1 m to 6.5 m s⁻¹. This corresponds to a Reynolds number of $Re = U_\infty d / \nu \in [0.3, 1.8] \times 10^4$ (ν the kinematic viscosity of air at working temperature) based on the diameter of the disk d or $Re_c = U_\infty d_c / \nu \in [1.4, 9.2] \times 10^2$ based on the diameter of the rod d_c .

Furthermore, as shown by the zoomed view near the disk (figure 1c), the static yaw angle β_0 for the disk is the second control parameter. Five main static yaw angles $\beta_0 = \{30, 40, 50, 60, 70\}^\circ$ are considered in the present study.

For each case in the (U_∞, β_0) parameter space, the instantaneous pendulum angle $\phi(t)$ is measured by a contactless digital encoder (Netzer DS-25 with 17-bit resolution) integrated into the air bushing system. All the measurements are conducted at a sampling rate of 2000 Hz. For the cases requiring statistical investigations, the data are recorded for 240 s when the free stream velocity is measured to be steady. This duration spans approximately 240 natural oscillation cycles of the pendulum, which is found to be satisfactory for statistical convergence.

For a time-dependent variable \mathcal{X} , the notation is defined as follows: $\bar{\mathcal{X}}$ represents the time-averaged value, $\sigma_{\mathcal{X}}$ denotes the standard deviation, and $\dot{\mathcal{X}}$ and $\ddot{\mathcal{X}}$ indicate the first and second time derivatives, respectively.

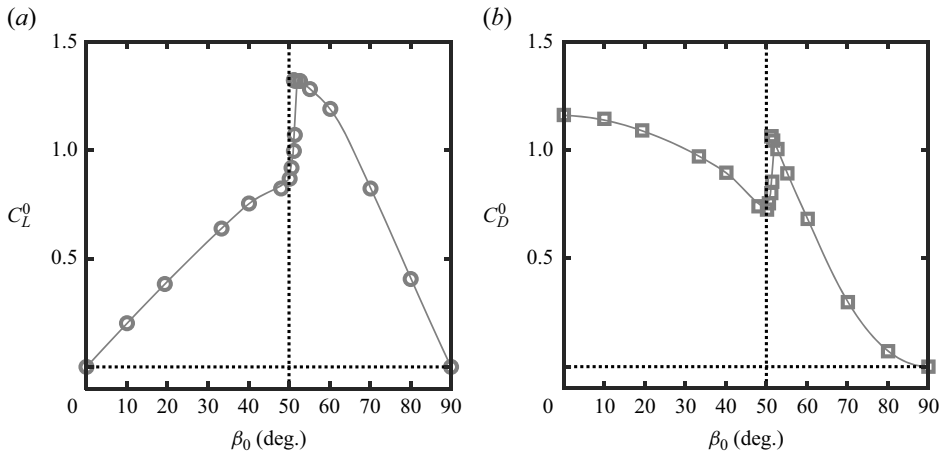


Figure 2. Mean lift C_L^0 and drag C_D^0 coefficients of a static disk measured by Flachsbart (1932).

2.2. Quasi-steady equation of motion of the system

In the framework of flow-induced vibration (FIV), the ratio between the advective frequency of the flow U_∞/d (d is the characteristic length of the body in the cross-flow direction) and the natural frequency of the system f_0 is a crucial parameter indicating the types of FIV that potentially occur. This parameter $U_r = U_\infty/(f_0d)$ is called the reduced velocity. When f_0 matches the vortex shedding frequency of the body, modal couplings such as vortex-induced vibration potentially occur. This typically happens for reduced velocities U_r ranging between 5 and 8 for 2-D bluff bodies (Blevins 1990). Furthermore, motion-induced vibration such as galloping happens in a wider range of U_r , with the lowest threshold governed by the mass and damping parameters of the system (Parkinson & Brooks 1961). The quasi-steady theory introduced by Den Hartog (1932) is often used for analysing the galloping instability, which is applicable typically when $U_r > 20$ (Blevins 1990).

For the parameter space of the present study, the reduced velocity U_r is calculated and is found to be larger than the threshold $U_r = 20$. Therefore, we present in this section a quasi-steady equation of motion of the pendulum. In addition, other non-stationary phenomena, in particular added mass effects (proportional to relative acceleration and relative density between the surrounding fluid and the pendulum), are also expected to be negligible owing to the large density ratio between the pendulum and the surrounding air. We therefore neglect all non-stationary contributions to the aerodynamic forces acting on it and simply consider a quasi-steady approximation for the aerodynamic forces (and the subsequent torques) acting on the disk and the rod.

First of all, the aerodynamic force acting on the disk is considered. As illustrated in figure 1(d), when the pendulum is moving at an angular velocity $\dot{\phi}$, the velocity at the centre of the disk is $V = L\dot{\phi}$. This additional relative motion between the disk and the surrounding air results in an apparent velocity having a magnitude of $U = \sqrt{U_\infty^2 + (L\dot{\phi})^2}$ and a dynamic yaw angle of $\beta = \beta_0 + \delta\beta$ with $\delta\beta = \arctan(L\dot{\phi}/U_\infty)$. The aerodynamic force components are the drag force F_D , acting in the direction of U , and the lift force F_L , acting perpendicular to the direction of U . They are defined as

$$F_D = 0.5\rho U^2 S C_D, \quad F_L = 0.5\rho U^2 S C_L, \quad (2.1)$$

where ρ is the density of the air, $S = \pi d^2/4$ is the area of the disk, C_D and C_L are the drag and lift coefficients, respectively. We emphasise that the aerodynamic coefficients C_L and C_D considered here do not display complex transient behaviour and follow quasi-statically the temporal evolution of the dynamic yaw angle $\beta(t)$, i.e. $C_L = C_L^0(\beta(t))$ and $C_D = C_D^0(\beta(t))$ with C_L^0 and C_D^0 the values of the aerodynamic coefficients obtained from the time-averaged force coefficients of a fixed disk at varying yaw angle as displayed in [figure 2](#) (Flachsbart 1932; Satheesh *et al.* 2022). Furthermore, the aerodynamic force component along the direction of motion F_ϕ can be determined by

$$F_\phi = F_L \cos(\delta\beta) - F_D \sin(\delta\beta) = 0.5\rho U^2 S C_\phi, \tag{2.2}$$

where $C_\phi = C_L \cos(\delta\beta) - C_D \sin(\delta\beta)$ is the force coefficient along the direction of motion. The aerodynamic torque from the disk Γ_ϕ then reads

$$\Gamma_\phi = F_\phi L. \tag{2.3}$$

Moreover, the aerodynamic torque from the cylindrical rod is also expressed. Along the rod, the local velocity at a position with a distance r from the pivot is $r\dot{\phi}$. The magnitude of the apparent velocity U_c and the dynamical yaw angle β_c at this position are expressed as $U_c = \sqrt{U_\infty^2 + (r\dot{\phi})^2}$ and $\beta_c = \delta\beta_c = \arctan(\frac{r\dot{\phi}}{U_\infty})$, respectively. The local force coefficient along the direction of motion $C_{\phi c}$ is determined by a combination of the local lift $C_{Lc} = C_{Lc}(\beta_c(t))$ and drag $C_{Dc} = C_{Dc}(\beta_c(t))$ coefficients:

$$C_{\phi c} = C_{Lc} \cos(\delta\beta_c) - C_{Dc} \sin(\delta\beta_c). \tag{2.4}$$

For Reynolds number of a few hundreds, a 2-D circular cylinder has a mean lift coefficient $C_{Lc}^0 \approx 0$ and a mean drag coefficient of $C_{Dc}^0 \approx 1$ according to the measurements by Wieselsberger (1922) and Tritton (1959). They are not dependent on the yaw angle. Following the quasi-steady approximation, we will consider $C_{Lc} = C_{Lc}^0$ and $C_{Dc} = C_{Dc}^0$ in this equation.

For an infinitesimal segment of the rod dr at a distance r from the pivot, the local aerodynamic torque contribution $d\Gamma_{\phi c}$ is

$$d\Gamma_{\phi c} = 0.5\rho U_c^2 d_c C_{\phi c} r \, dr. \tag{2.5}$$

By integrating $d\Gamma_{\phi c}$ along the exposed part of the rod to the free stream, the aerodynamic torque on the rod is expressed as

$$\Gamma_{\phi c} = \int_{r_{min}}^{r_{max}} d\Gamma_{\phi c}. \tag{2.6}$$

Taking into account the aerodynamic torques derived above and the gravitational torque, the equation of motion of the system reads

$$J\ddot{\phi} = -mgl\sin(\phi) + \Gamma_\phi + \Gamma_{\phi c}. \tag{2.7}$$

This equation of motion, with the expression of the torques given by relations (2.3) and (2.6), will be used in § 3 to explain the dynamical properties measured for the pendulum. The relative importance of the various torque terms will also be discussed for the Pendulum and Windmill states. Finally, in § 4, this equation will be the main building block of a simple model of the observed dynamical features.

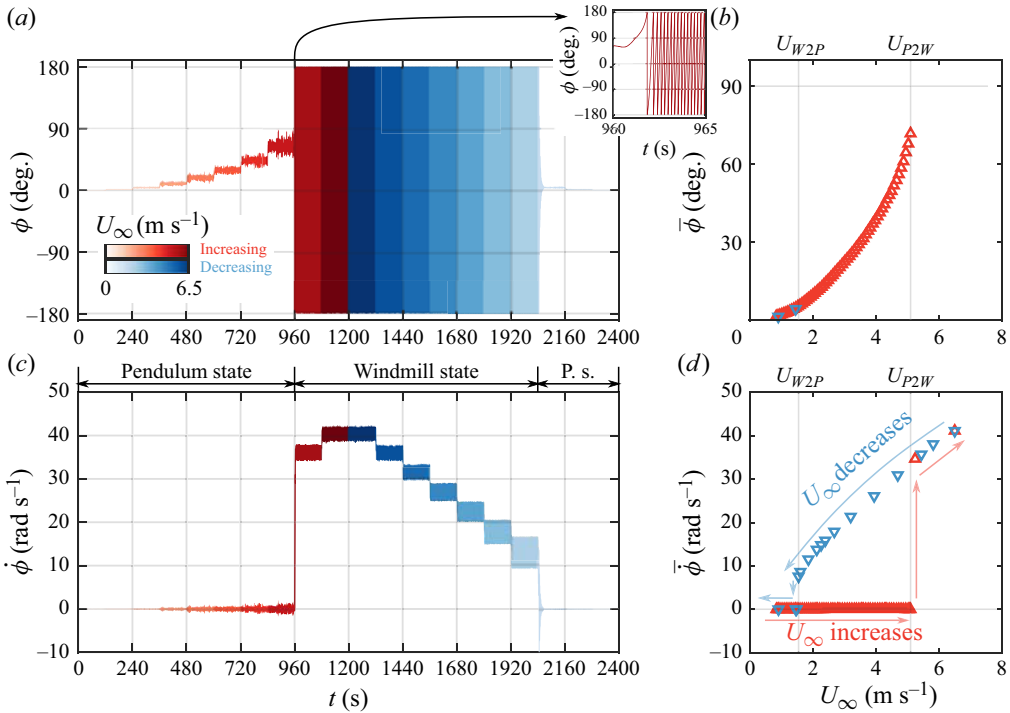


Figure 3. For configuration $\beta_0 = 40^\circ$: (a, c) time evolution of the pendulum angle ϕ and the angular velocity $\dot{\phi}$, the free stream velocity U_∞ is first increased and then decreased in a stepwise manner ($\Delta U_\infty = 0.7 \text{ m s}^{-1}$, step length $T_{step} = 120 \text{ s}$); (b, d) evolution of the mean pendulum angle $\bar{\phi}$ and the mean angular velocity $\bar{\dot{\phi}}$ with increasing (Δ , coloured in red) and decreasing (∇ , coloured in blue) U_∞ , U_{P2W} and U_{W2P} denote respectively the transition U_∞ from Pendulum to Windmill state and from Windmill to Pendulum state.

3. Experimental investigation of the dynamics

In this section, we present the main important features observed experimentally regarding the pendulum behaviour at various yaw angles when the free stream velocity is cycled (first increased then decreased). We first show a hysteretic behaviour with the existence of two main states in § 3.1, namely the Pendulum and Windmill states, and then we investigate the angular dynamics of the system in each of these states in § 3.2.

3.1. Overview of the evolution of the dynamics with the free stream velocity

We present in figure 3(a) the time evolution of the pendulum angle ϕ for the configuration $\beta_0 = 40^\circ$, when the free stream velocity U_∞ is varied step by step ($\Delta U_\infty = 0.7 \text{ m s}^{-1}$). Here, U_∞ is first increased (coloured in red) and then decreased (coloured in blue) in a stepwise manner (step length $T_{step} = 120 \text{ s}$). The mean pendulum angle $\bar{\phi}$ increases with U_∞ for $U_\infty < 5 \text{ m s}^{-1}$ (i.e. $0 < t < 960 \text{ s}$ in figure 3(a)). This is shown also in figure 3(b) by the evolution of the mean pendulum angle $\bar{\phi}$ with U_∞ with a smaller U_∞ step size ($\Delta U_\infty = 0.1 \text{ m s}^{-1}$). In this state, as shown in figure 3(a), the angular fluctuations around the mean pendulum angle $\bar{\phi}$ increase with U_∞ . As U_∞ is further increased above a critical value $U_{P2W} \simeq 5 \text{ m s}^{-1}$ ($960 < t < 1200 \text{ s}$), the pendulum first moves to the uppermost location ($\phi = 180^\circ$) and then starts to rotate (see the inset in figure 3(a)). The rotation of the pendulum persists with decreasing U_∞ ($1200 < t < 2040 \text{ s}$), and then stops when U_∞ is further decreased below a critical value $U_{W2P} \simeq 2 \text{ m s}^{-1}$ ($t > 2040 \text{ s}$). The system then

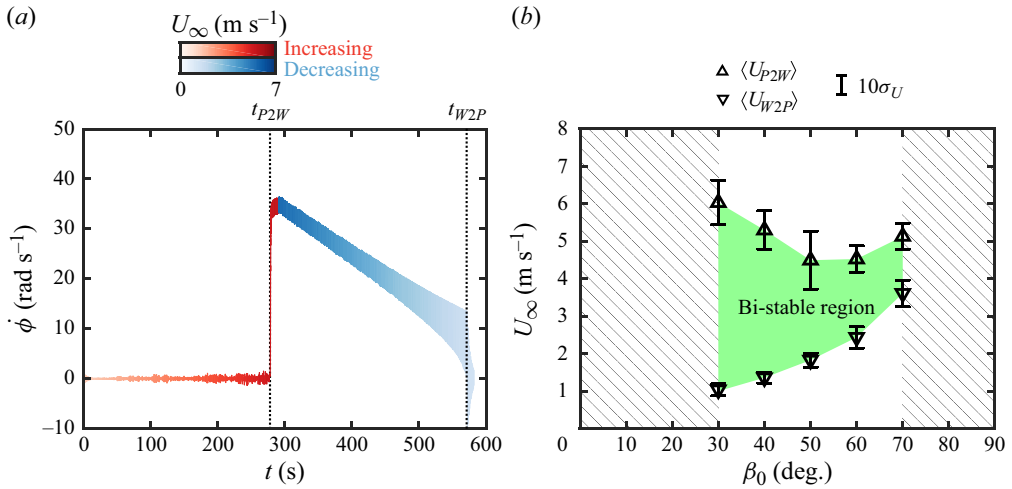


Figure 4. (a) Time evolution of $\dot{\phi}$ for configuration $\beta_0 = 40^\circ$, U_∞ is first increased and then decreased in a continuous manner at a constant speed $|dU_\infty/dt| = 0.015 \text{ m s}^{-2}$. (b) For approximately 100 repetitions (each β_0 configuration) of the procedure in (a), variations of the mean $\langle U \rangle$ and standard deviations σ_U of the transition velocities (U_{P2W} and U_{W2P}) with β_0 .

recovers the features of the pendulum state observed for $0 < U_\infty < U_{P2W}$. We refer to the non-rotating state as the Pendulum state and to the rotating state as the Windmill state, and hence the notation U_{P2W} and U_{W2P} for the critical velocities for which transitions are observed between these two states. Note the fact that $U_{W2P} < U_{P2W}$ reveals a hysteretic behaviour, with a bi-stability when $U_{W2P} < U_\infty < U_{P2W}$, further explored in the rest of this article.

Figure 3(c) shows the time evolution of angular velocity $\dot{\phi}$, computed as the time derivative of the signal $\phi(t)$ displayed in figure 3(a). The evolution of the mean angular velocity $\bar{\phi}$ with U_∞ , computed for each step of constant free stream velocity U_∞ , is plotted in figure 3(d). As U_∞ increases from 0 (red points and red arrows in figure 3d), we first observe that the mean angular velocity remains equal to zero, i.e. the system does not rotate and is in the Pendulum state. The abrupt transition to the rotating Windmill state, with a finite average value of the angular velocity, is observed for the velocity $U_{P2W} \simeq 5 \text{ m s}^{-1}$. Starting from the Windmill state, and as U_∞ is decreased (blue points and blue arrows in figure 3d), the Windmill state is sustained over the bi-stable zone with decreasing values of $\bar{\phi}$, until a transition towards the Pendulum state as $U_\infty = U_{W2P} \simeq 2 \text{ m s}^{-1} < U_{P2W}$ for the configuration with $\beta_0 = 40^\circ$.

Before presenting a detailed description of dynamics in each state in § 3.2, we first focus here on the dependencies of the critical velocities U_{P2W} and U_{W2P} , and of the bi-stability range on the static yaw angle β_0 . The two critical transition velocities are statistically quantified for given values of the static yaw angle β_0 (between 30° and 70°) by using a different experimental protocol. Instead of adjusting U_∞ in a stepwise manner, we first increase and then decrease it continuously at a constant rate of $|dU_\infty/dt| = 0.015 \text{ m s}^{-2}$. As shown in figure 4(a), the critical velocities U_{P2W} and U_{W2P} are then determined from the abrupt transitions detected on the signal of angular velocity $\dot{\phi}$. For each β_0 configuration, approximately 100 individual samples of U_{P2W} or U_{W2P} are then acquired by repeating the protocol. In figure 4(b), the ensemble-averaged values $\langle U_{P2W} \rangle$ and $\langle U_{W2P} \rangle$ of the samples are summarised for different β_0 configurations. We note that $\langle U_{P2W} \rangle$ is always larger than $\langle U_{W2P} \rangle$. This means that the bi-stable region exists for all

the β_0 configurations considered in this study. Furthermore, we observe that the velocity range of the bi-stable region gradually decreases with increasing β_0 . We also observe that while the Windmill-to-Pendulum critical velocity U_{W2P} is a monotonically increasing function of the yaw angle β_0 , the Pendulum-to-Windmill critical velocity U_{P2W} is non-monotonic and has a minimum for $\beta_0 \simeq 50^\circ$, which is close to the stall angle of an inclined disk (Flachsbart 1932). The existence of this minimum point suggests that the Pendulum-to-Windmill transition appears to be facilitated near stall.

The standard deviation of the transition velocities σ_U (estimated from the variability of U_{P2W} and U_{W2P} over the 100 transitions detected for each configuration) is also presented in figure 4(b), which gives information on the nature of the transitions. Here, σ_U is magnified by 10 times ($10\sigma_U$) in the figure to compare different β_0 configurations. For all the β_0 configurations, the standard deviation of U_{P2W} is larger than that of U_{W2P} . Furthermore, we notice that the standard deviation of U_{P2W} is maximum when $\langle U_{P2W} \rangle$ is minimum (for $\beta_0 \simeq 50^\circ$). However, the standard deviation of U_{W2P} increases monotonically with increasing β_0 . Altogether, these observations suggest that the Pendulum-to-Windmill transition is eased when the static yaw angle β_0 is close to the stall angle of the disk and its triggering may be promoted by enhanced aerodynamic fluctuations in such a configuration. However, no particular connection is observed between stall/fluctuations and the Windmill-to-Pendulum transition, suggesting that the transition from the Windmill state to the Pendulum state may be more deterministic.

The different transition behaviours will be further discussed and explained in § 4 with the help of a stochastic model describing the system dynamics. This protocol described above is used as a compromise between a reasonable duration of the experimental campaign and enough samples to quantify the transition velocities. However, it is important to note here that such a protocol may induce non-stationary effects, which have been shown to influence the apparent threshold of saddle-node bifurcation (Kogan 2007; Kim, Harne & Wang 2017; Kim & Wang 2018). Therefore, for the rest of the paper, we focus on the protocol using a stepwise evolution of U_∞ rather than a sweeping variation of U_∞ . We make sure that the duration of the step is sufficient to reach a permanent state.

3.2. Detailed dynamical features of the Pendulum and Windmill states

The dynamics of the system in the Pendulum and Windmill states, regarding the mean value and the temporal fluctuation of the angular position and angular velocity, are now described separately.

3.2.1. Dynamics of the Pendulum state

Mean pendulum angle. The evolution of the mean angle $\bar{\phi}$ with the free stream velocity U_∞ is shown in figure 5(a) (restricted to the Pendulum state, i.e. for $U_\infty < U_{P2W}(\beta_0)$). For all β_0 configurations, $\bar{\phi}$ gradually increases as U_∞ increases. However, the increase rate is strongly dependent on the value of β_0 . This is better depicted in figure 5(b), showing the variations of $\bar{\phi}$ with β_0 at four different free stream velocities $U_\infty = \{1.09, 2.15, 2.94, 3.82\} \text{ m s}^{-1}$ marked by the vertical dashed lines in figure 5(a).

Figure 5(b) shows that as U_∞ increases, a sudden change in slope at $\beta_0 \simeq 50^\circ$ progressively emerges. In addition, a peak at $55^\circ < \beta_0 < 60^\circ$ becomes more obvious. This trend can qualitatively be interpreted in the frames of the quasi-static approximation for the aerodynamic forces acting on the disk and of the stall transition of the lift coefficient of a thin disk. Indeed, in the quasi-static approximation presented in § 2.2, the average equilibrium position of the system in the Pendulum state can be expressed by

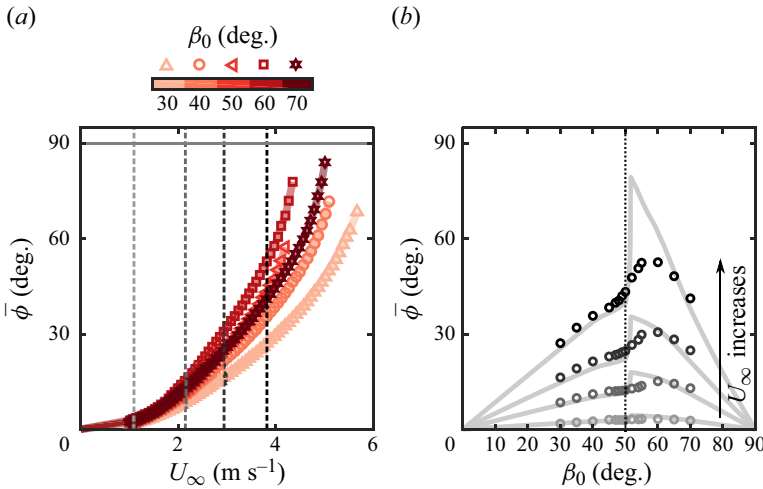


Figure 5. Pendulum state: (a) variations of $\bar{\phi}$ with U_∞ for different β_0 configurations; (b) variations of $\bar{\phi}$ with β_0 at different $U_\infty = \{1.09, 2.15, 2.94, 3.82\}$ m s⁻¹ marked by dashed lines in (a), mean pendulum angle calculated from (3.3) using reference cross-flow force coefficient for an inclined static disk from Flachsbarth (1932) are shown by lines for comparison.

the time-averaged torque balance derived from (2.7):

$$\overline{\Gamma_{\phi c}} + \overline{\Gamma_\phi} = mgl\overline{\sin(\phi)}. \quad (3.1)$$

The mean torque of the rod holding the disk $\overline{\Gamma_{\phi c}}$ is neglected first, as for symmetry reasons, it is not expected to have any net average contribution. Furthermore, the mean aerodynamic torque from the disk $\overline{\Gamma_\phi} = 0.5\rho U^2 C_\phi(\beta)SL$ can be approximated by the main lift contribution associated with the mean free stream $0.5\rho U_\infty^2 \overline{C_L(\beta)}SL$, owing to the fact that we experimentally noticed that the maximum velocity of the pendulum is one order of magnitude smaller than the free stream velocity ($\max(L\dot{\phi}) \lesssim 0.1U_\infty$), hence $\cos(\delta\beta) \simeq 1$ and $\sin(\delta\beta) \simeq 0$. The equilibrium condition can then be considered as the balance between the torque of weight and the aerodynamic lift torque from the mean free stream as a reasonable dominant aerodynamic contribution (given that the pendulum is constrained here to oscillate in a plane perpendicular to the free stream):

$$0.5\rho U_\infty^2 \overline{C_L(\beta)}SL = mgl\overline{\sin(\phi)}. \quad (3.2)$$

Here, we have also used the approximation $\overline{\sin(\phi)} \approx \overline{\sin(\bar{\phi})}$ (which is expected since we consider small excursions from the equilibrium position and has been experimentally verified to be accurately satisfied). It should also be noted here that $\overline{C_L(\beta)}$ can be linearised around the static yaw angle β_0 as $C_L(\beta_0) + \delta\beta \frac{dC_L}{d\beta}|_{\beta_0}$, where the second term is negligible except possibly near stall conditions where the lift coefficient may experience abrupt dependencies on the yaw angle (i.e. $|\frac{dC_L}{d\beta}|$ may be arbitrarily large as shown in figure 1e). Overall, it is therefore expected that for a given experimental configuration in the parameter space (β_0, U_∞), the average equilibrium condition in the Pendulum state shall be reasonably given by the balance between the torque of the weight and the torque of the lift from the main free stream U_∞ at the static yaw angle β_0 ,

$$0.5\rho U_\infty^2 C_L(\beta_0)SL = mgl\overline{\sin(\bar{\phi})}, \quad (3.3)$$

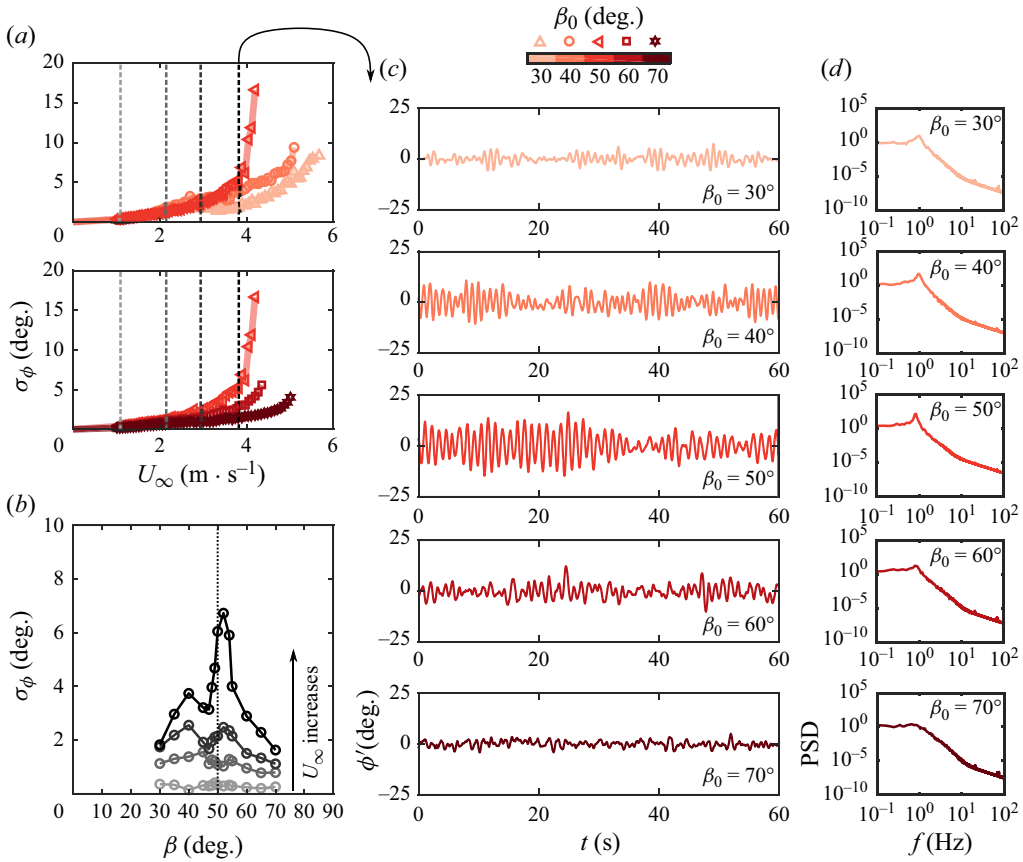


Figure 6. Pendulum state: (a, b) evolution of the standard deviation of the pendulum angle σ_ϕ with U_∞ for $\beta_0 \leq 50^\circ$ (top) and for $\beta_0 \geq 50^\circ$ (bottom); (b) variations of σ_ϕ with β_0 at different $U_\infty = \{1.09, 2.15, 2.94, 3.82\}$ m s $^{-1}$ marked by dashed lines in (a); (c) time evolution of the pendulum angle fluctuation $\phi' = \phi - \bar{\phi}$ and (d) the corresponding power spectral density (PSD) for several values of β_0 at $U_\infty = 3.82$ m s $^{-1}$.

except possibly when the static yaw angle lies in the vicinity of stall conditions. This balance is tested in figure 5(b), where we extract the value of $\bar{\phi}$ using (3.3) with the U_∞ values and the reference measurements of the lift coefficient of a fixed disk (Flachsbart 1932). The agreement with experimental measurements is overall quantitatively very good, except in the vicinity of stall where only a qualitative trend is recovered. However, this qualitative agreement confirms the fact that the sudden increase of the mean angular position $\bar{\phi}$ observed in the vicinity of stall is a signature of the strong increase of the static lift coefficient for β_0 between 50° and 60° .

Fluctuations of the pendulum angle. The increase of the fluctuations of the pendulum angle around the time-averaged value with U_∞ was briefly introduced in figure 3(a). Figure 6 displays a detailed characterisation of these angular fluctuations. The evolution of the standard deviation of the pendulum angle σ_ϕ with the free stream velocity U_∞ is first shown in figure 6(a). For all the configurations, an increase of σ_ϕ with U_∞ is observed. However, the amplitude of the fluctuations strongly depends upon the value of the yaw angle β_0 . The configuration $\beta_0 = 50^\circ$ (in the vicinity of stall) presents large amplitude fluctuations, with σ_ϕ reaching $\sim 15^\circ$. For all other configurations, the standard deviation

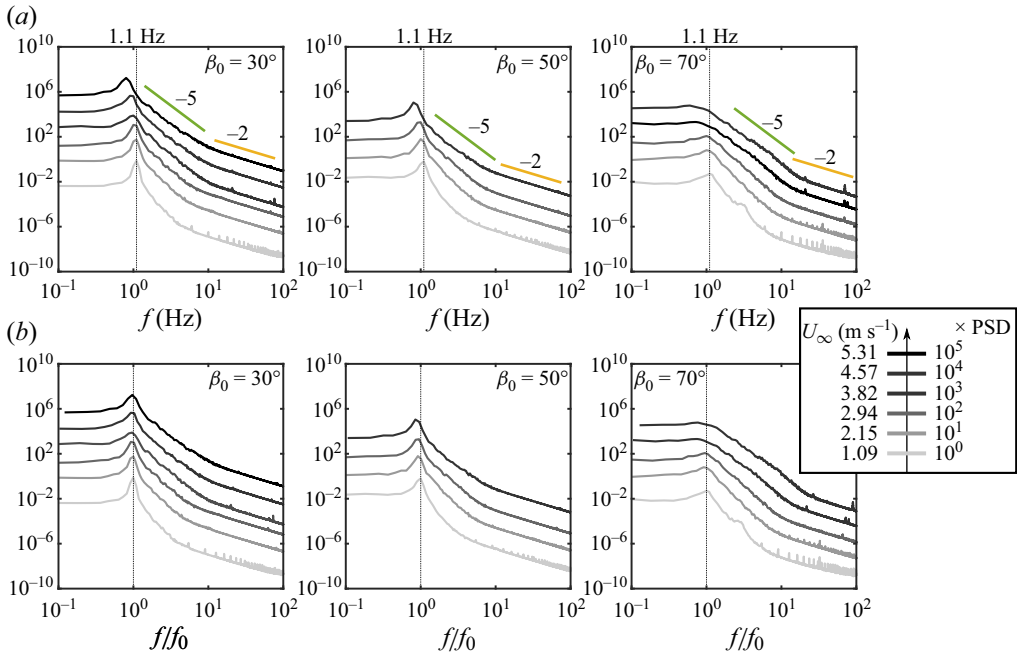


Figure 7. Pendulum state: (a) variations of the PSD of the pendulum angle with U_∞ , (b) the same spectra as (a) but plotted against f/f_0 (f_0 is the natural frequency of the pendulum).

σ_ϕ is below 10° . Refined evolution of σ_ϕ with the static yaw angle β_0 is presented in figure 6(b) for four different free stream velocities $U_\infty = \{1.09, 2.15, 2.94, 3.82\} \text{ m s}^{-1}$ as marked by vertical dashed lines in figure 6(a). The fluctuation level sharply rises in the vicinity of stall for $\beta_0 \approx 50^\circ$, in particular for the highest values of the free stream velocity. As will be discussed later in § 4.3, this non-monotonic dependency of pendulum angle fluctuation on β_0 is important in triggering the transition from the Pendulum to the Windmill state and, therefore, is crucial in setting the Pendulum-to-Windmill transition velocity shown before in figure 4(b).

The time series of the pendulum angle fluctuation $\phi' = \phi - \bar{\phi}$ for different values of β_0 at $U_\infty = 3.82 \text{ m s}^{-1}$ are reported in figure 6(c). For configurations with $\beta_0 \leq 50^\circ$, a clear signature of the natural frequency of the pendulum is observed, with phases of quiet periods alternating with more intense fluctuations. This translates in the presence of a strong peak at ~ 1 Hz on the corresponding power spectral density (PSD) in figure 6(d). However, the signature of the natural frequency oscillations is significantly damped for the configurations with $\beta_0 > 50^\circ$ and the time evolution appears more random. This is also evident in the PSD where the peak at ~ 1 Hz observed for $\beta_0 \leq 50^\circ$ configurations is progressively reduced. For configuration $\beta_0 = 70^\circ$, the peak is not distinguishable with a flat PSD below $f = 1$ Hz, characteristic of large-scale random dynamics with no dominant frequency.

The evolution of the PSD with U_∞ is shown in figure 7(a) for three values of β_0 . For all the configurations above the peak at $f \approx 1$ Hz, the PSD decreases rapidly as f^{-5} and then as f^{-2} . This suggests that the system efficiently dissipates high-frequency fluctuating energy. Furthermore, the oscillation peak at $f \approx 1$ Hz is observed for all the cases with $\beta_0 \leq 50^\circ$, while it begins to emerge with reducing U_∞ for configuration $\beta_0 = 70^\circ$. Finally, a collapse of the peaks is observed in figure 7(b) when the frequency is

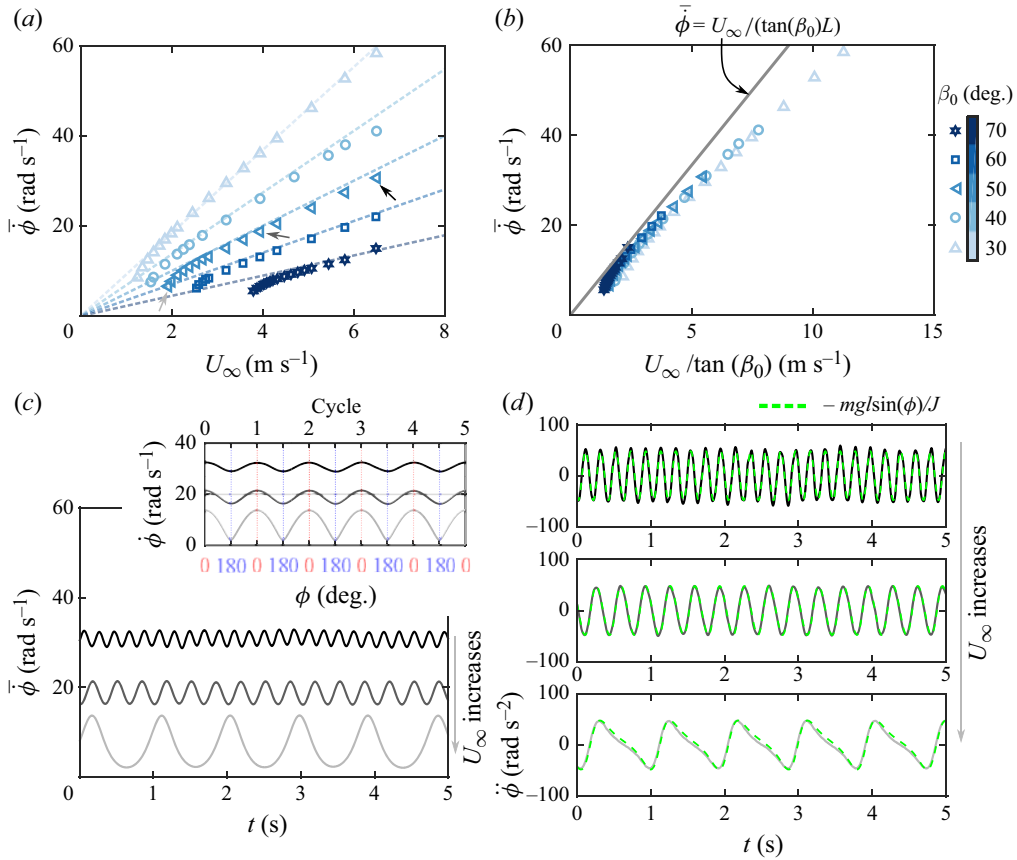


Figure 8. Windmill state: (a) evolution of $\bar{\dot{\phi}}$ with U_∞ for different β_0 configurations, see text for details; (b) comparison of the experimental results with the prediction neglecting the drag of the rod $\tan(\beta_0) = U_\infty / (L\bar{\dot{\phi}})$. Time evolution of (c) the rotation speed $\dot{\phi}$ and (d) the angular acceleration $\ddot{\phi}$ for the cases highlighted by arrows in (a). Inset of (c) shows the evolution of $\dot{\phi}$ against ϕ for five rotation cycles.

rescaled by the natural frequency of the pendulum $f_0 = \frac{1}{2\pi} \sqrt{\frac{mgl}{J} \cos(\bar{\phi})}$ (which depends on the equilibrium angles $\bar{\phi}$), showing that the fluctuations of the pendulum angle are mainly driven by its natural frequency.

3.2.2. Dynamics of the Windmill state

Average rotation rate. For all the cases in the Windmill state, the evolution of the mean rotation velocity $\bar{\dot{\phi}}$ with the free stream velocity U_∞ is shown for different β_0 configurations in figure 8(a). We observe that at high free stream velocities, the mean rotation velocity $\bar{\dot{\phi}}$ grows linearly with U_∞ , with a slope that increases when the static yaw angle β_0 decreases. This linear behaviour is lost as the free stream velocity is decreased and the mean rotation velocity reduces below approximately 10 rad s⁻¹, when the Windmill state becomes unsustainable and the system returns to the Pendulum state.

We will now explain the origin of the linear dependency of $\bar{\dot{\phi}}$ on U_∞ . This can be interpreted by writing the time-averaged torque balance derived from (2.7):

$$\overline{\Gamma_\phi} + \overline{\Gamma_{\phi c}} = mgl \overline{\sin(\phi)} = 0. \tag{3.4}$$

The mean gravitational torque $mgL\overline{\sin(\phi)}$ is zero owing to its periodicity in the Windmill state. This mean torque balance simply translates the equilibrium between aerodynamic lift acting on the disk (included in $\overline{\Gamma_\phi}$) and the aerodynamic drag, part of which acts on the disk (and is included in $\overline{\Gamma_\phi}$) and on the cylindrical rod holding it (represented by $\overline{\Gamma_{\phi_c}}$). Based on this force balance, the linear dependency of $\overline{\dot{\phi}}$ on U_∞ can be simply inferred for this balance by noting that, if fluctuations of $\dot{\phi}$ (and hence of the dynamical yaw angle $\beta = \beta_0 + \delta\beta$) are neglected, then the total average aerodynamic torque $\overline{\Gamma_\phi} + \overline{\Gamma_{\phi_c}}$ can be written as a sole function of β_0 and $L\overline{\dot{\phi}}/U_\infty$ (and of the fixed geometrical parameters of the system: L , L_c , d and d_c). The balance in (3.4) therefore reduces to solving

$$f_{geom}(L\overline{\dot{\phi}}/U_\infty, \beta_0) = 0, \tag{3.5}$$

where f_{geom} is a function that depends on the system geometry. For a given value of the static yaw angle β_0 , it trivially follows that $\overline{\dot{\phi}}$ is linearly proportional to U_∞ . The function f_{geom} cannot be derived analytically, but (3.5) can be solved numerically for all values of β_0 explored experimentally. These solutions are shown as dashed lines in figure 8(a). We note that at relatively high angular velocities ($\overline{\dot{\phi}} > 10 \text{ rad s}^{-1}$), the experimental results follow nicely the linear relationship, suggesting that the rotation velocity $\dot{\phi}$ can be considered as a constant for these cases. This argument will be further justified later by looking at the time evolution of $\dot{\phi}$ over the different experimental configurations.

Before exploring the variability of the rotation rate in the next paragraph, we briefly discuss here the role of the drag on the cylindrical rod in the average rotation rate. The aerodynamic torque from the rod Γ_{ϕ_c} may indeed seem negligible at first sight, due to its small diameter (5 % of the diameter of the disk). However, this is not the case. Indeed, by neglecting the aerodynamic torque from the rod in (3.4) and then in (3.5), the simpler condition $\overline{\Gamma_\phi} = 0$ connects the rotation velocity $\overline{\dot{\phi}}$ and the free stream velocity U_∞ via the so-called velocity triangle condition, a terminology used very often in the field of turbomachinery (Venkanna 2009; Turton 2012), which here simply results in

$$\overline{\dot{\phi}} = \frac{U_\infty}{\tan(\beta_0)L}. \tag{3.6}$$

In other words, this condition expresses the idea that a steady rotation state corresponds to a vanishing of the dynamic yaw angle β for the disk considering its relative motion to surrounding air flow. The experimental results are compared in figure 8(b) with this simplified scenario. We observe that the linear behaviour predicted for the angular rotation relative to the free stream velocity when the drag on the cylindrical rod is neglected overestimates the actual average rotation speed $\overline{\dot{\phi}}$, which is measured to be always smaller than the situation matching the velocity triangle condition. This difference increases with increasing U_∞ when β_0 is fixed, showing a gradually enhanced influence from the rod on the mean rotation speed.

Variability of the rotation rate. For three cases highlighted by arrows in figure 8(a), the time series of the instantaneous angular velocity $\dot{\phi}(t)$ are shown in figure 8(c). This clearly shows that the rotation speed is not steady, but subject to a strong regular modulation. The amplitude of this modulation is found to increase when reducing U_∞ . In addition, the inset of figure 8(a) shows that this modulation occurs every revolution of the pendulum and is due to the effect of gravity on the unbalanced pendulum: the torque of the weight tends to accelerate the pendulum when it moves downwards and to decelerate it when it moves upwards.

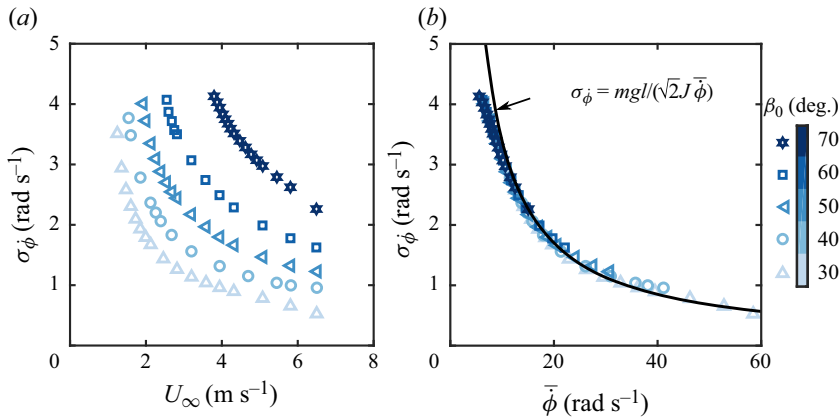


Figure 9. Evolution of the standard deviation of the angular velocity $\sigma_{\dot{\phi}}$ in the Windmill state (a) as a function of U_{∞} , and (b) as a function of $\bar{\phi}$.

To further quantify the effect of gravity, the instantaneous angular acceleration $\ddot{\phi}(t)$ is shown in figure 8(d) for the three cases presented in figure 8(c) and is compared with the instantaneous contribution of gravity $mgl \sin \phi(t)/J$. The quasi-perfect superposition of both quantities shows the leading role of gravity on the rotation modulation.

For all the cases in the Windmill state, the modulation effect of gravity is further investigated by showing the standard deviation of the angular velocity $\sigma_{\dot{\phi}}$ in figure 9(a). It is noticed that $\sigma_{\dot{\phi}}$ presents a hyperbolic relationship with U_{∞} . It is then found in figure 9(b) that the mean rotation velocity $\bar{\phi}$ is the correct scaling parameter for $\sigma_{\dot{\phi}}$, which collapses all the β_0 configurations. Such a hyperbolic relationship $\sigma_{\dot{\phi}} \sim 1/\bar{\phi}$ may be interpreted by neglecting the effect of aerodynamics on the pulsation of rotation velocity. Under such a situation, the maximum (minimum) rotation velocity $\dot{\phi}_{max}$ ($\dot{\phi}_{min}$) happens at $\phi = 0^\circ$ (180°). The relationship between these two rotation velocities is linked by the kinetic energy balance

$$0.5J\dot{\phi}_{max}^2 - 0.5J\dot{\phi}_{min}^2 = mg2l, \tag{3.7}$$

translating the transfer between kinetic and potential energy over each pendulum revolution. We approximate the time evolution of $\dot{\phi}$ as a sine wave, which is a rough approximation when the mean rotation velocity is smaller than 10 rad s^{-1} (see figure 8c for the smallest velocity). The balance between the kinetic and the potential energy is then rewritten as

$$2mgl = 0.5J(\dot{\phi}_{max} - \dot{\phi}_{min})(\dot{\phi}_{max} + \dot{\phi}_{min}) = 0.5J(2\bar{\phi})(2\sqrt{2}\sigma_{\dot{\phi}}). \tag{3.8}$$

This hyperbolic relationship $\sigma_{\dot{\phi}} = mgl/(\sqrt{2J}\bar{\phi})$ follows, in good agreement with the experimental results as shown in figure 9(b). Interestingly, the transfer between potential and kinetic energy implies a simple relation between the average and the standard deviation of the rotation velocity: $\bar{\phi}\sigma_{\dot{\phi}} = K_{geom}$, where K_{geom} is a constant that depends on the geometry of the system. A slight difference between the relationship and the experimental results is noticed when $\bar{\phi} < 10 \text{ rad s}^{-1}$. This is probably because $\dot{\phi}$ does not evolve in a sine wave as expected when making the approximation.

We have shown that in the Windmill state, the average rotation rate is primarily driven by aerodynamic forces (through (3.4)), while the pulsation of the rotation velocity is mainly driven by the modulation effect of gravity, which is gradually weakened as the mean rotation velocity is increased. At small rotation velocity $\bar{\dot{\phi}} < 10 \text{ rad s}^{-1}$, the strong modulation effect leads to a large variation in $\dot{\phi}$. The variation in $\dot{\phi}$ has a strong effect on the mean rotation velocity $\bar{\dot{\phi}}$ and cannot be simply neglected. However, at large rotation velocity $\bar{\dot{\phi}} > 10 \text{ rad s}^{-1}$, the modulation effect is limited and the rotation velocity can be reasonably considered as steady, which justifies the analysis made in the previous paragraphs to infer the linearity between $\bar{\dot{\phi}}$ and U_∞ .

4. Stochastic modelling of the dynamics

This section is dedicated to a discussion of the main results presented, in particular regarding the stochastic and deterministic behaviours of the system, its bifurcations and bi-stability. In particular, the results presented in previous sections show that while the dynamics of the system in the Pendulum state may exhibit erratic fluctuations, the Windmill state shows much more regular dynamics. The possible influence of such random fluctuations on the dynamics in each state and the transitions between states therefore need to be addressed. With this perspective, we propose a simple model for simulating the role of random noise on the system dynamics. Based on this model, we then give further insights into the state transitions of the system.

To address the possible role of noisy fluctuations (whose origins may lay in the turbulent wake of the disk, or in incident fluctuations of the free stream), we consider the equation of motion already introduced in § 2.2, to which we add a random source term $\sigma_n \xi$:

$$J\ddot{\phi} = -mgl \sin(\phi) + \Gamma_\phi + \Gamma_{\phi c} + \sigma_n \xi. \tag{4.1}$$

Here, σ_n is the noise intensity, and ξ is a random delta correlated signal with normal distribution and a standard deviation $\sigma_\xi = 1$. Using the angular dependency of the quasi-static aerodynamic force coefficients from Flachsbart (1932) for the disk and a mean drag coefficient $C_{Dc} = 1$ for the cylindrical rod (Wieselsberger 1922; Tritton 1959), this stochastic model is now examined in the Pendulum and Windmill states, respectively.

4.1. Modelling the features of the Pendulum state

In the Pendulum state, the stochastic model is further linearised to investigate the response of the system to noise, as proposed recently by Myskiw *et al.* (2024) for a cube pendulum. Briefly, from the average equilibrium position $\bar{\phi}$, the consideration of a small angular displacement $\epsilon = \phi - \bar{\phi}$ allows the linearisation of (4.1) which gives

$$\ddot{\epsilon} + \frac{\rho SL^2 U_\infty}{2J} H \dot{\epsilon} + \frac{mgl}{J} \cos(\bar{\phi}) \epsilon = \frac{\sigma_n \xi}{J}, \tag{4.2}$$

where H is the aerodynamic damping coefficient and is written as

$$H = C_D(\beta_0) - \left. \frac{dC_L}{d\beta} \right|_{\beta_0} + \frac{d_c \int_{r_{min}}^{r_{max}} r^2 dr}{SL^2} C_{Dc}. \tag{4.3}$$

Note here that the aerodynamic force from the cylindrical rod is taken into account. The relationship between H and the static yaw angle β_0 is shown in figure 10(a) calculated using the mean aerodynamic coefficients for the disk from Flachsbart (1932) (see figure 1e).

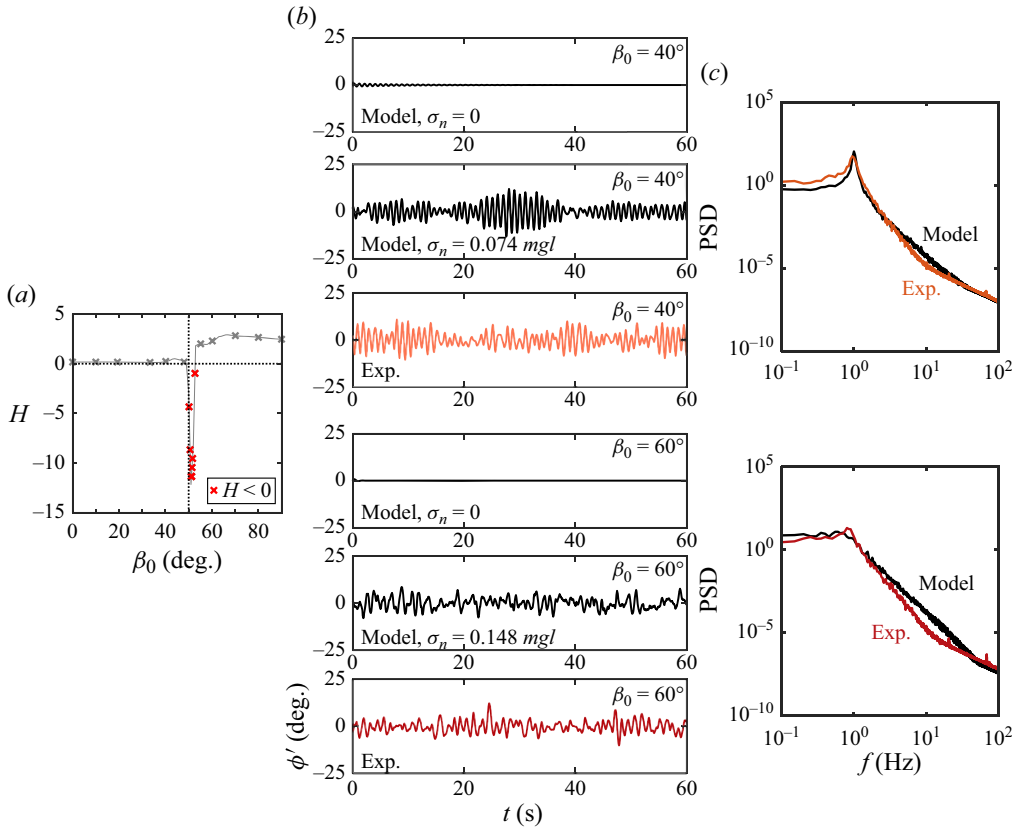


Figure 10. Modelling of the dynamics in the Pendulum state: (a) reduced aerodynamic damping coefficient H of the system calculated using the mean aerodynamic coefficients of the disk for different static yaw angle β_0 from Flachsbart (1932) (see figure 2e); (b) time evolution and (c) the corresponding spectrum from the nonlinear stochastic model (4.1) and experiments for different β_0 at $U_\infty = 3.82 \text{ m s}^{-1}$, different noise amplitudes σ_n are considered for the model.

Let us first discuss the β_0 ranges, $\beta_0 < 50^\circ$ and $\beta_0 > 50^\circ$, for which the aerodynamic damping H is positive. A small value of H is observed for $\beta_0 < 50^\circ$, while larger values are obtained for $\beta_0 > 50^\circ$. This is mainly driven by the sign of $\frac{dC_L}{d\beta}|_{\beta_0}$ which reverses at stall. This difference in aerodynamic damping level explains the different angular responses shown before in figure 6.

In the vicinity of stall, the sharp evolution of C_L with β_0 leads to a negative damping coefficient H when estimated from static aerodynamic coefficients (Flachsbart 1932). This suggests that the system is unstable when β_0 is close to the stall angle and is potentially subject to the galloping instability (Den Hartog 1932, 1956). This is in accordance with the experimental measurements shown in figure 6(b), where a peak in the pendulum angle fluctuations is noticed near stall. However, we note that the response of the system at $\beta_0 = 50^\circ$, as shown before in figure 6(c), although it presents important oscillations at the natural frequency, is still very different from the typical highly regular galloping response at high reduced velocities (Zhao, Hourigan & Thompson 2018; Zhang *et al.* 2024). We suggest that this difference is primarily caused by the strong flow unsteadiness near stall, reminiscent of the dynamic stall for 2-D aerofoils (McCrosky 1981; Mulleners & Raffel 2013). Preliminary measurements suggest the existence of dynamical stall for a forced

oscillating disk. Therefore, a description of the dynamics near stall does require accurately modelling the unsteadiness of the aerodynamic coefficients, which is beyond the reach for the present investigation. In the following, we will focus on the modelling of pendulum dynamics away from stall.

Now, we focus in [figure 10\(b\)](#) on the stochastic modelling of the system dynamics in the Pendulum state for $\beta_0 = 40^\circ$ and 60° , respectively below and above the stall angle. [Figure 10\(b\)](#) displays the experimental time series of the pendulum angle fluctuation $\phi' = \phi - \bar{\phi}$ as well as the results of the numerical simulations of the stochastic model (4.1) in the absence and in the presence of noise. The simulations are initialised by starting from $\phi = 0^\circ$ and $\dot{\phi} = 0 \text{ rad s}^{-1}$ mimicking the experimental situation when the free stream velocity U_∞ is increased from zero. A proper value of the noise intensity σ_n is adjusted to ensure that the simulated fluctuations of the pendulum angle σ_ϕ have the same standard deviation as in the experiments, which is of the order of $\sigma_n \sim 0.1mgl$. As expected, a finite level of noise is required to observe fluctuations on the simulations reported in [figure 10\(b\)](#), with a noise amplitude of the order of the fluctuations of the gravitational term $mgl\sin(\phi)$. We note that the fine-tuned noise level, σ_n , is doubled for the configuration $\beta_0 = 60^\circ$ compared with $\beta_0 = 40^\circ$. This is consistent with previous observation by Obligado *et al.* (2013) using a disk pendulum free to rotate in a plane parallel to the free stream, showing a greater sensitivity of aerodynamic torque to free stream turbulence in configurations with $\beta_0 \geq 60^\circ$ compared with those with $\beta_0 \leq 40^\circ$. Finally, in [figure 10\(b\)](#), we note that the relatively more regular (random) oscillation for the $\beta_0 = 40^\circ$ (60°) configuration is well simulated. This is further confirmed by the nice collapse in the PSD of the angular fluctuations shown in [figure 10\(c\)](#), in particular, regarding the damping of the natural frequency peak for $\beta_0 = 60^\circ$ compared with the case $\beta_0 = 40^\circ$.

4.2. Modelling the dynamics in the Windmill state

Let us first recall that, in the Windmill state, the variation of the gravitational term $mgl\sin(\phi)$ due to the rotation is one order of magnitude higher than that in the Pendulum state, while we expect the aerodynamic fluctuations to be of the same order of magnitude for both states. We checked that the dynamical features in the Windmill state are correctly reproduced in the absence of the noise term in (4.1), thus leading to a deterministic model for the Windmill state. The difference between a deterministic simulation and a stochastic simulation (with a small noise amplitude) leads to no observable difference in the time evolution of the rotation velocity. All simulations reported in the present section are therefore deterministic (i.e. $\sigma_n = 0$ in (4.1)).

The experimental results in the Windmill state previously reported in [figures 8\(a\)](#) and [8\(c\)](#) are reproduced in [figure 11](#) and are compared with the simulation results. The initial condition for the simulations is set to $\phi = 0^\circ$ and $\dot{\phi} = 60 \text{ rad s}^{-1}$, which is similar to the experimental situation when U_∞ is gradually decreased. For all the cases in the Windmill state, we note that the model captures the rotatory dynamics very adequately. [Figure 11\(a\)](#) highlights the capacity of the model to reproduce the instantaneous evolution of the rotation speed and [figure 11\(b\)](#) shows that the time-averaged mean angular velocity $\bar{\dot{\phi}}$ is also very well captured by the model. The fact that a deterministic model reproduces all the features of the Windmill state suggests that, experimentally, the dynamics in the Windmill state are more immune to the presence of noise due to aerodynamics, which is in accordance with the more deterministic nature of the Windmill-to-Pendulum transition measured in [figure 4](#). We will further explore in the next subsection the nature of the transitions between Pendulum and Windmill states.

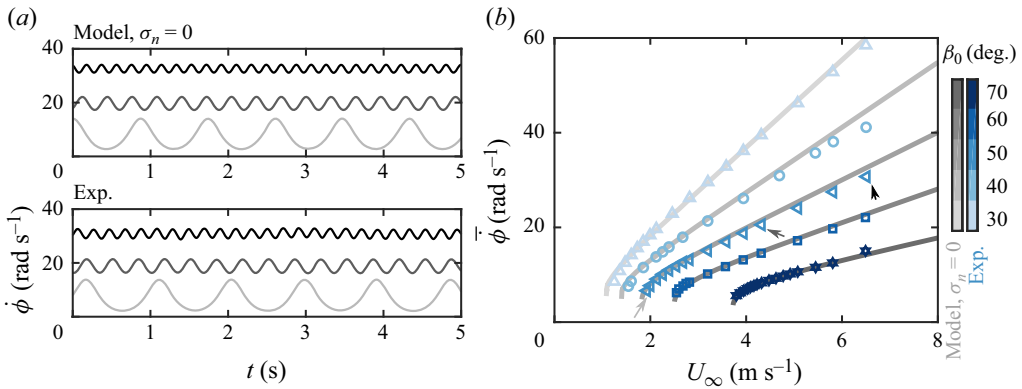


Figure 11. Modelling of the dynamics in the Windmill state: (a) time evolution of $\dot{\phi}$ and (b) evolution of the mean rotation velocity $\dot{\phi}$ as a function of U_{∞} from the nonlinear stochastic model (4.1) and experiments. The cases shown in (a) are highlighted by arrows in (b).

4.3. Nature of the transitions between the Pendulum and the Windmill states

We start analysing the Pendulum-to-Windmill transition by neglecting first the fluctuations of the angular position of the pendulum around its equilibrium position (i.e. assuming $\dot{\phi} = 0$), hence in a deterministic scenario of the transition. This assumption (which will be further discussed below) may appear reasonable at first sight since the experimental data in the Pendulum state shows that, though the spectral content of the fluctuations is rich (as previously illustrated in figure 10), the maximum velocity of the pendulum oscillations is one order of magnitude smaller than the free stream velocity ($\max(L\dot{\phi}) \sim 0.1U_{\infty}$). Under this assumption, we consider the equilibrium scenarios in the Pendulum state sketched in figure 12(a) for different mean free stream conditions. When $U_{\infty} = 0$ (no aerodynamic torque is exerted on the disk, $\Gamma_{\phi} = 0$), the system has two equilibrium positions: a stable one $\phi_s = 0$ and an unstable one $\phi_u = \pi$. As U_{∞} increases, the aerodynamic forces gradually move the two equilibrium positions towards $\pi/2$. Indeed, when the mean aerodynamic force is smaller than the weight torque ($\Gamma_{\phi} < mgl$), the two equilibrium positions are $\phi_s = \arcsin(\Gamma_{\phi}/(mgl))$ and $\phi_u = \pi - \phi_s$. When the aerodynamic force attains the threshold $\Gamma_{\phi} = mgl$, the two solutions collide and a saddle-node bifurcation is expected towards the Windmill state, as no fixed equilibrium exists when the mean aerodynamic torque exceeds the weight torque, with $\Gamma_{\phi} > mgl$.

In this deterministic transition scenario, the Pendulum state is sustained if the pendulum locates around ϕ_s and the transition to Windmill state should occur for the deterministic critical velocity $U_{\infty} = U_{P2W}^{\det}$ such that $\Gamma_{\phi} = mgl$ and $\bar{\phi} = \pi/2$. However, as reported in figure 5(a), it is experimentally observed that the transition to the Windmill state is systematically anticipated compared with this scenario and occurs for experimental conditions at which the mean angular position prior to transition is $\bar{\phi} < \pi/2$, hence the actual transition threshold $U_{P2W} < U_{P2W}^{\det}$. This reflects the non-deterministic nature of the Pendulum-to-Windmill transition and the triggering role of angular fluctuations to promote oscillations passing the unstable position of the pendulum even if the conditions are not met for the stable and unstable steady equilibrium points to collide at $\pi/2$.

The relevance of this scenario is supported by figure 12(b), which represents the temporal signal of angular position fluctuations for two different values of the mean free stream such that $U_{\infty} < U_{P2W}$ and $U_{\infty} = U_{P2W}$ (for the case $\beta_0 = 40^\circ$). The horizontal solid lines in these plots represent respectively the average stable equilibrium position

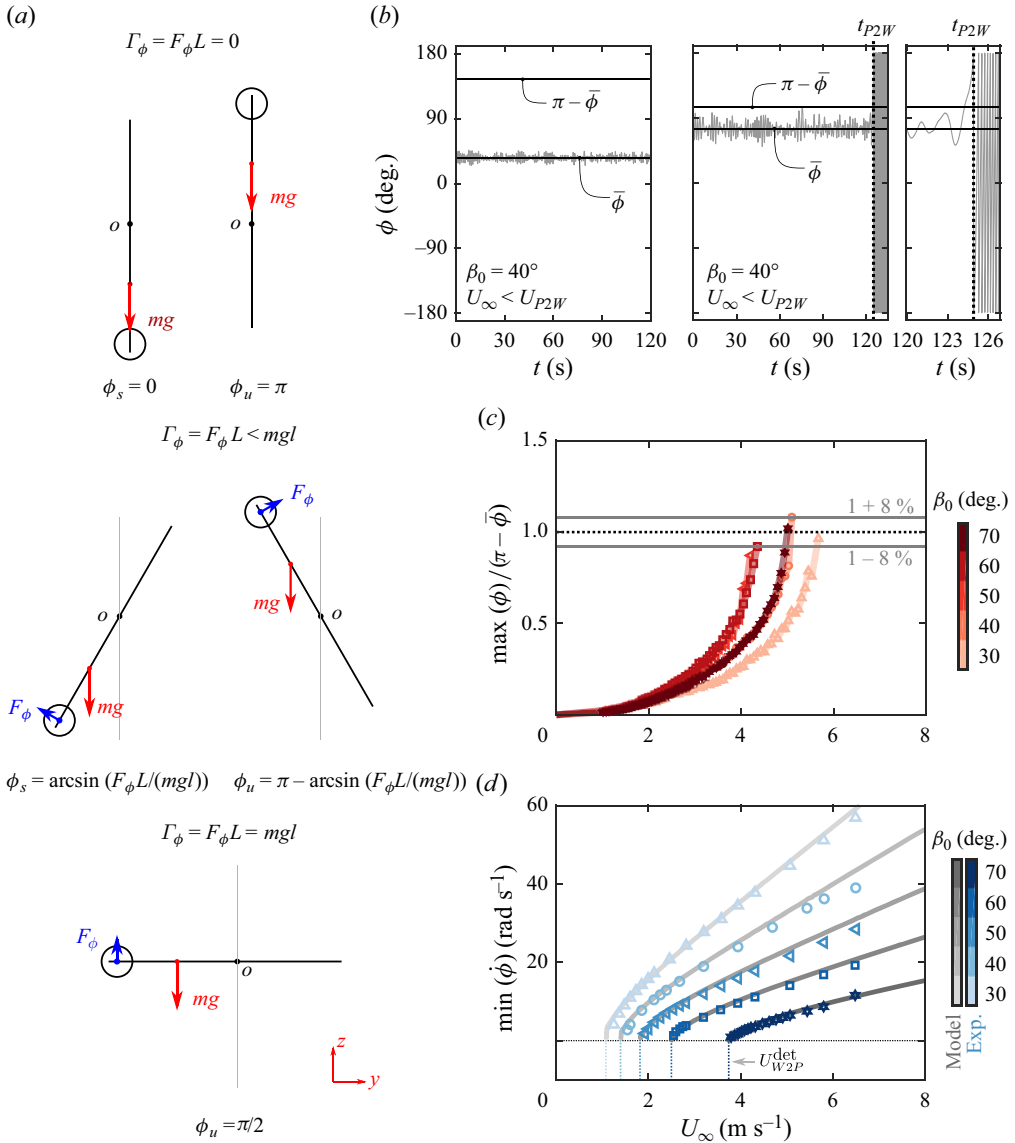


Figure 12. (a) Stable ϕ_s and unstable ϕ_u fixed points for increasing mean aerodynamic moments F_ϕ^*L (or equivalently increasing U_∞) from top to bottom in the Pendulum state. (b) Time evolution of the pendulum angle ϕ for $\beta_0 = 40^\circ$ (left) below and (right) at the Pendulum-to-Windmill transition velocity U_{P2W} . (c) Evolution of $\max(\phi) / (\pi - \bar{\phi})$ with U_∞ for all available experimental cases in the Pendulum state. (d) Minimum of the angular velocity $\min(\dot{\phi})$ in the Windmill state for all experimental cases and for the model.

$\bar{\phi}$ and the average corresponding unstable position $\pi - \bar{\phi}$. It can be seen that below the threshold ($U_\infty < U_{P2W}$), the stable and unstable equilibrium positions are separated enough to prevent the angular fluctuations of the pendulum around its stable position to approach the unstable position. The transition to the Windmill state occurs at the critical velocity $U_\infty = U_{P2W}$ for which the stable equilibrium position $\bar{\phi} < \pi/2$ (meaning that $U_{P2W} < U_{P2W}^{\det}$) and the peaks of fluctuations do approach the unstable position. The ansatz can therefore be formulated that the condition for the transition can be written

as $\max(\phi) \approx \pi - \bar{\phi}$. To test the relevance of this condition, we plot in figure 12(c) the quantity $\max(\phi)/(\pi - \bar{\phi})$ for all β_0 cases we explored, as a function of U_∞ up to the transition threshold U_{P2W} . It can be observed that the transition threshold accurately corresponds to the condition $\max(\phi)/(\pi - \bar{\phi}) = 1 \pm 8\%$, which validated the proposed condition and the phenomenology that the Pendulum-to-Windmill transition is anticipated by the fluctuations compared with the deterministic prediction.

We have seen in §§ 3.2.2 and 4.2 that the Windmill state dynamics is quite regular, and overall faithfully reproduced by the deterministic model, without the noise term. In particular, we have observed that the rotation rate $\dot{\phi}$ of the pendulum is modulated by the weight imbalance with a maximum value $\dot{\phi}_{max}$ when $\phi = 0$ (the pendulum being at its most downwards position) and a minimum value $\dot{\phi}_{min}$ when $\phi = \pi$ (the pendulum being at its most upwards position). The amplitude of the modulation increases as the free stream velocity U_∞ decreases, up to the point where $\dot{\phi}_{min}$ vanishes and the cycle over the upwards position cannot be sustained anymore, which defines the Windmill-to-Pendulum threshold U_{W2P} . Figure 12(d) represents the minimum rotation rate $\dot{\phi}_{min}$ determined from the experiments for all the explored parameters (symbols) and for the numerical resolution of the deterministic equation of motion ((4.1) with $\sigma_n = 0$). The agreement is very good, in particular near the Windmill-to-Pendulum transition, where $\dot{\phi}_{min} \rightarrow 0$. The minimum U_∞ required to sustain rotation differs by at most 0.16 m s^{-1} between the experimental results and the model across all configurations. This confirms that the Windmill-to-Pendulum transition is primarily deterministic and the threshold is accurately predicted using a deterministic model ($U_{W2P} = U_{W2P}^{det}$).

5. Concluding remarks

In this article, we reported a detailed experimental characterisation of the dynamics of a disk pendulum swept by a flow and free to rotate in the direction perpendicular to the flow. The system exhibits two states: a pendulum state, static on average and subject to strong aerodynamic fluctuations, and a regularly rotating windmill state. Subcritical bifurcations between these states, as well as bi-stability, were observed for all values of the static yaw angle of the disk β_0 . The features of the time-averaged characteristics in both states are faithfully captured using a quasi-steady approach with aerodynamic coefficients measured for fixed disks (Flachsbar 1932). The dynamical features and the nature of the transitions were also explored using a stochastic model based on the quasi-steady approach with additive noise. In the Pendulum state, this model accurately reproduces all dynamical features for the cases far from the stall angle. In particular, the variation in system behaviour for yaw angles, especially the more regular dynamics below the stall angle compared with the irregularities above, are shown to be linked to the concavity of the aerodynamic lift curve $C_L(\beta_0)$. Moreover, this model also validates the experimental observations that the bifurcation from the Pendulum state to the Windmill state is triggered by aerodynamic fluctuations. However, the features of the Windmill state are faithfully captured by a fully deterministic quasi-steady model (i.e. no additive noise is required). This also endorses the deterministic nature of the Windmill-to-Pendulum bifurcation observed.

The goal of the present work was to reveal and investigate the two different states, the bi-stability and the nature of the transitions between the states. We have shown that a quasi-steady description accurately captures most of the features of the pendulum bi-stable dynamics for yaw angles far from stall. In contrast, the present experimental data near stall is not well described by this quasi-steady approach. Further investigations for yaw angles close to the stall angle would be required to explore whether transient phenomena such

as dynamic stall or transient detachment–attachment of the wake structure would help to improve the predictions. In particular, dedicated time-resolved flow visualisations of the wake structure in the Pendulum state or precise embedded pressure measurements would help clarifying these issues in the vicinity of the stall angle.

This study adds to previous investigations showing that a configuration as simple as a pendulum in a flow displays non-trivial behaviours (Obligado *et al.* 2013; Gayout *et al.* 2021). Moreover, this configuration, where the pendulum freely rotates in the cross-flow plane, could be a test bed for investigating stochastic processes in multi-stable systems. The influence of more complex geometries could be investigated. The influence of asymmetric damage on the dynamics of rotating systems would, for instance, be easy to probe. Finally, this canonical configuration is also appealing for detailed studies on the influence of extreme aerodynamic events or of the amplitude (and characteristic correlation time) of the free stream turbulent fluctuations, for instance, using active-grid generated fluctuations.

Acknowledgements. The authors would like to warmly thank M. Moulin, P. Metz, J. Miniot, J. Pereda, J.-M. Breux and F. Paillé for invaluable support during experiments, C. Sicot and S. Bera for insightful discussions, J. Borée and Y. Haffner for critical reading and useful comments.

Funding. We are indebted to the French Agence Nationale de la Recherche (ANR) through the ANR project Turb-Cab (ID ANR-22-CE220010) for financial support.

Declaration of interests. The authors report no conflict of interest.

Author contributions. All authors contributed equally to data curation, methodology, software, validation and writing, review and editing. N.P. and M.B. shared equal responsibilities for conceptualisation, funding acquisition, project administration and resource management. D.B. was solely responsible for investigation, supervision, visualisation and drafting the original manuscript. Formal analysis was conducted by all authors, with D.B. taking the lead.

REFERENCES

- BANDI, M.M., CONCHA, A., WOOD, R. & MAHADEVAN, L. 2013 A pendulum in a flowing soap film. *Phys. Fluids* **25** (4), 041702.
- BLEVINS, R. 1990 *Flow-Induced Vibration*. 2nd edn. Krieger.
- BOS, R.W. & WELLENS, P.R. 2021 Fluid-structure interaction between a pendulum and monochromatic waves. *J. Fluids Struct.* **100**, 103191.
- CARBERRY, J. & SHERIDAN, J. 2007 Wake states of a tethered cylinder. *J. Fluid Mech.* **592**, 1–21.
- DEN HARTOG, J.P. 1932 Transmission line vibration due to sleet. *Trans. Am. Inst. Electrical Engrs* **51** (4), 1074–1076.
- DEN HARTOG, J.P. 1956 *Mechanical Vibrations*. McGraw-Hill.
- FANI, A. & GALLAIRE, F. 2015 The motion of a 2d pendulum in a channel subjected to an incoming flow. *J. Fluid Mech.* **764**, 5–25.
- FLACHSBART, V.O. 1932 Messungen an ebenen und gewölbten platten. In *Ergebnisse der Aerodynamischen Versuchsanstalt zu Göttingen*, IV., 4th edn. (ed. L. PRANDTL), pp. 96–100. Verlag von R. Oldenbourg.
- GAYOUT, A., BOURGOIN, M. & PLIHON, N. 2021 Rare event-triggered transitions in aerodynamic bifurcation. *Phys. Rev. Lett.* **126** (10), 104501.
- GOLD, T., REITERER, K., WORF, D., KAIBLINGER, N., KHOSRONEJAD, A., HABERSACK, H. & SINDELAR, C. 2024 Dynamics of heavy subaqueous spherical pendulums. *J. Fluid Mech.* **978**, A19.
- GONG, X. & QIAO, W. 2012 Imbalance fault detection of direct-drive wind turbines using generator current signals. *IEEE Trans. Energy Convers.* **27** (2), 468–476.
- GOVARDHAN, R. & WILLIAMSON, C.H.K. 1997 Vortex-induced motions of a tethered sphere. *J. Wind Engng Ind. Aerodyn.* **69**, 375–385.
- GOVARDHAN, R.N. & WILLIAMSON, C.H.K. 2005 Vortex-induced vibrations of a sphere. *J. Fluid Mech.* **531**, 11–47.
- KIM, J., HARNE, R.L. & WANG, K.W. 2017 Predicting non-stationary and stochastic activation of saddle-node bifurcation. *J. Comput. Nonlinear Dyn.* **12** (1), 011009.

- KIM, J. & WANG, K.W. 2018 Predicting non-stationary and stochastic activation of saddle-node bifurcation in non-smooth dynamical systems. *Nonlinear Dyn.* **93** (2), 251–258.
- KOGAN, O. 2007 Controlling transitions in a duffing oscillator by sweeping parameters in time. *Phys. Rev. E* **76** (3), 037203.
- KOVALEV, D., ESHBAL, L. & VAN HOUT, R. 2022 Three-dimensional flow field measurements in the wake of a tethered sphere crossing the onset of vortex induced vibrations. *J. Fluid Mech.* **943**, A37.
- LUGT, H.J. 1983 Autorotation. *Ann. Rev. Fluid Mech.* **15** (1), 123–147.
- MATHAI, V., LOEFFEN, L.A.W.M., CHAN, T.T.K. & WILDEMAN, S. 2019 Dynamics of heavy and buoyant underwater pendulums. *J. Fluid Mech.* **862**, 348–363.
- MCCROSKY, W.J. 1981 The phenomenon of dynamic stall. *NASA Tech. Rep.* 81264.
- MULLENERS, K. & RAFFEL, M. 2013 Dynamic stall development. *Exp. Fluids* **54** (2), 1–9.
- MYSKIW, A., HAFFNER, Y., PAILLÉ, F., BORÉE, J. & SICOT, C. 2024 One-degree-of-freedom galloping instability of a 3d bluff body pendulum at high reynolds number. *J. Fluids Struct.* **127**, 104123.
- NEILL, D., LIVELYBROOKS, D. & DONNELLY, R.J. 2007 A pendulum experiment on added mass and the principle of equivalence. *Am. J. Phys.* **75** (3), 226–229.
- OBLIGADO, M., PUY, M. & BOURGOIN, M. 2013 Bi-stability of a pendular disk in laminar and turbulent flows. *J. Fluid Mech.* **728**, R2.
- ORCHINI, A., KELLAY, H. & MAZZINO, A. 2015 Galloping instability and control of a rigid pendulum in a flowing soap film. *J. Fluids Struct.* **56**, 124–133.
- PARKINSON, G.V. & BROOKS, N.P.H. 1961 On the aeroelastic instability of bluff cylinders. *J. Appl. Mech.* **28** (2), 252–258.
- RAJAMUNI, M.M., THOMPSON, M.C. & HOURIGAN, K. 2019 Vortex-induced vibration of elastically-mounted spheres: a comparison of the response of three degrees of freedom and one degree of freedom systems. *J. Fluids Struct.* **89**, 142–155.
- RAJAMUNI, M.M., THOMPSON, M.C. & HOURIGAN, K. 2020 Vortex dynamics and vibration modes of a tethered sphere. *J. Fluid Mech.* **885**, A10.
- RAMAMURTHY, A.S. & LEE, P.M. 1973 Wall effects on flow past bluff bodies. *J. Sound Vib.* **31** (4), 443–451.
- RAMLAU, R. & NIEBSCH, J. 2009 Imbalance estimation without test masses for wind turbines. *J. Sol. Energy Engng* **131** (1), 1–7.
- RUIZ, T., SICOT, C., BRIZZI, L.E., LAUMONIER, J., BORÉE, J. & GERVAIS, Y. 2009 Unsteady near wake of a flat disk normal to a wall. *Exp. Fluids* **47** (4), 637–653.
- RYAN, K., PREGNALATO, C.J., THOMPSON, M.C. & HOURIGAN, K. 2004 Flow-induced vibrations of a tethered circular cylinder. *J. Fluids Struct.* **19** (8), 1085–1102.
- RYAN, K., THOMPSON, M.C. & HOURIGAN, K. 2007 The effect of mass ratio and tether length on the flow around a tethered cylinder. *J. Fluid Mech.* **591**, 117–144.
- SATHEESH, S., SPOHN, A., KERHERVÉ, F. & CORDIER, L. 2022 Drag regimes of circular discs at different inclinations. *Ocean Engng* **266**, 112931.
- SEMIN, B., DECOENE, A., HULIN, J.-P., FRANÇOIS, M.L.M. & AURADOU, H. 2012 New oscillatory instability of a confined cylinder in a flow below the vortex shedding threshold. *J. Fluid Mech.* **690**, 345–365.
- STOKES, G.G. 1850 On the effect of the internal friction of fluids on the motion of pendulums. *Trans. Camb. Phil. Soc.* **9**, 8–106.
- TRITTON, DAVID J. 1959 Experiments on the flow past a circular cylinder at low reynolds numbers. *J. Fluid Mech.* **6** (4), 547–567.
- TURTON, R.K. 2012 *Principles of Turbomachinery*. Springer.
- VENKANNA, B.K. 2009 *Fundamentals of Turbomachinery*. PHI Learning Pvt.
- WIESELSBERGER, C. 1922 New data on the laws of fluid resistance. *NACA Tech. Rep.* TN-84.
- ZHANG, C., TANG, G., LU, L., JIN, Y., AN, H. & CHENG, L. 2024 Flow-induced vibration of two tandem square cylinders at low reynolds number: transitions among vortex-induced vibration, biased oscillation and galloping. *J. Fluid Mech.* **986**, A10.
- ZHAO, J., HOURIGAN, K. & THOMPSON, M.C. 2018 Flow-induced vibration of d-section cylinders: an afterbody is not essential for vortex-induced vibration. *J. Fluid Mech.* **851**, 317–343.